

Electrochemo-mechanical Properties of Red Phosphorus Anodes in Lithium, Sodium and Potassium-ion Batteries

Isaac Capone¹, Jack Aspinall¹, Ed Darnbrough¹, Ying Zhao², Tae-Ung Wi³, Hyun-Wook Lee³, and Mauro Pasta^{1,*}

¹Department of Materials, University of Oxford, Parks Road, Oxford OX1 3PH, United Kingdom

²Department of Aerospace Engineering and Applied Mechanics, Tongji University, 100 Zhangwu Road, 200092 Shanghai, China

³School of Energy and Chemical Engineering, Ulsan National Institute of Science and Technology (UNIST), Ulsan, South Korea

*Corresponding author: mauro.pasta@materials.ox.ac.uk

Abstract

Red phosphorus (RP) is a promising anode material for alkali-ion batteries due to a high theoretical capacity at low potentials when alloying with lithium, sodium and potassium. Most alloy anode materials display large volume changes during cycling which can lead to particle fracturing, low coulombic efficiency, loss of electrical contact and ultimately poor cycle life. In this paper we outline, through comprehensive electrochemo-mechanical characterisation and modelling of the cycling stresses, why RP can be cycled at high current densities without fracture. Novel application of in-situ nanoindentation and powder compression to battery materials allows for measurement of the elastic, plastic and fracture properties of RP. Modelling shows that the stresses from Na and K alloying are greater than Li and that particle geometry is important to stress concentration. This model is tested through in-situ TEM observation with extreme conditions (anisotropic ion diffusion and high current density), observing no catastrophic failure of RP particles with any ion. The combination of mechanical, electrochemical characterisation with geometry and stress modelling allows for predictions to be made for application of RP in alkali-ion batteries.

Introduction

As Li-ion battery (LIB) production capacity increases, the cost per kWh will be ever more dictated by the cost of raw materials. Investigation to find a low cost, high energy density materials is therefore a priority[1–3]. Red phosphorus (RP) satisfies this brief with the added unique interest of alloying with multiple alkali-ions.

RP, the amorphous allotrope of phosphorus, is globally abundant, has low processing temperatures and alloys successfully with lithium, sodium (theoretical capacity = 2596 mA h g⁻¹) and potassium

(theoretical capacity = 865 mA h g⁻¹). The alloying onset potential is well above the alkali metal plating potentials, enabling safe, high-power operation. As a result there is a growing number of publications studying this material as an anode in Li, Na and K-ion batteries [4–6]. RP, unlike other allotropes, is stable in air up to 260 C and so has reduced safety/flammability concerns for large scale production.[7]

Alloy anodes have been thoroughly investigated after Dey demonstrated the effective electrochemical alloying of lithium with many metals [8]. The intrinsically large volume expansions during alloying

are observed to lead to delamination from the current collector and self-pulverisation of the material. In the past two decades, anode architectures have been designed to accommodate much of the expansion to reduce the magnitude of stress. Architectures include complex host structures with voids to accommodate expansion, nanosized particles, core-shell nanoparticles and hollow nanoparticles [9–11]. The architecture with the greatest industrial relevance for lithium is the nanostructured graphite anode architecture comprising nanoparticles embedded within a graphite matrix [12]. Lui et al showed reducing the starting particle size, to the nanoscale, reduced the likelihood of fracture, but at the cost of increasing the surface area to volume ratio.[13] The exposed surface forms SEI, leading to impractical first cycle coulombic efficiency. [14] Accumulated evidences have shown that cyclic charge and discharge of LIBs give rise to various mechanical degradation at different length and time scales, including particle cracking and pulverization, SEI formation and fragmentation, particle debonding from matrix, electrode fracture, buckling and wrinkling. [15] Some of those degradation mechanisms are irreversible and can develop with each cycle, which contributes considerably to deterioration of battery electrochemical performance. [16] For instance, microcracks inside particles and solid electrolytes can increase the tortuosity of lithium diffusion pathways, leading to increased impedance of battery cell. [17, 18] Further developed cracks will introduce isolated particle fragments or unnecessary exposure of active materials to the electrolyte, causing eventually capacity fade and power loss. [19]

A number of strategies have been applied to RP in the hopes to avoid these effects and enhance the cyclability of the material. For example particle size reduction, via ball milling, is widely reported with RP and to form RP/C composites.[20–22] Another method that involves the sublimation and recrystallization of RP at high temperatures has also proven to be an effective way to produce stable electrodes, thanks to the ability of producing phosphorus nanoparticles embedded in a carbon matrix. [23, 24] Despite widespread application of these methods and the increasing numbers of works on RP, the relationship between the mechanical properties of RP, its particle size and the electrochemical performance is still not clear.

Therefore, mechanically informed understanding is key to the development of phosphorus-based electrode materials.

This paper gives a complete characterisation of the failure mode (departure from elasticity) of RP and utilises models (backed by experiment) to apply this information to electrodes design.

Electrochemo-mechanics

Alkali metal alloying and de-alloying of a RP particle leads to, among other phenomena, volumetric expansion and stress generation that ultimately leads to a short cycle life. The stresses generated inside the particle are related to the mechanical properties of RP (i.e. Young’s modulus E and Poisson’s ratio ν), ion diffusivity of alkali metal in the particle (D), partial molar volume of the alkali metal ion in RP (Ω), charge/discharge current density (i), as well as the initial particle shapes and sizes. The stresses in a stand-alone spherical particle with radius R_0 under homogeneous current across the particle surface can be obtained analytically from the electrochemo-mechanical model outlined in section 2 of [15] and reported in the Supporting Information (section 1). As the alloying reaction proceeds, the partial molar volume of the alkali metal ion in RP increases, giving rise to a volumetric chemical strain. Assuming a linear relationship between volume change and alkali metal concentration x (constant partial molar volume of A in A_xP) the corresponding hydrostatic stress around the particle core can be calculated. The principle stresses, i.e. the radial stress σ_r (the stress towards or away the centre point of the object) and the hoop stress σ_t (the stress perpendicular to the radius of the object), are both proportional to the same material properties as:

$$\sigma_r, \sigma_t \propto \frac{\Omega E}{1 - \nu} \frac{i R_0}{D} \quad (1)$$

Detailed expressions for σ_r and σ_t are reported in the Supporting Information (equations S4, S5).

Particles will experience mode I crack (a crack that is formed when the tensile stress is perpendicular to the plane of the crack) once these stresses overshoot the critical stress σ_{1C} of the particle. The critical stress is dependent on the fracture toughness, K_{1C} of the material:

$$\sigma_{1C} = \frac{K_{1C}}{\Psi \sqrt{2\pi r}} \quad (2)$$

where r is the flaw size acting as a stress concentrator and Ψ the crack geometry factor of order one.

In order to calculate the strain occurring in RP particles upon alloying, D , E and ν are needed. These values, to the authors' knowledge, are missing from the current literature. This work conducted a number of tests to measure the values needed for the above calculation. Secondly it will act as a substantial reference for the field going forwards adding to the previously reported bulk moduli values [25, 26].

Electrochemical properties

The diffusivities of Li^+ , Na^+ and K^+ in RP, as a function of the state of charge, were estimated using the galvanostatic intermittent titration technique (GITT) [27] and are reported in figure 1. Detailed experimental conditions are described in the Methods section and in the Supporting Information. Given the slow current applied in this procedure, we assume that the complete alloying of RP has occurred and the phases Li_3P , Na_3P and KP were formed.

The initial Li^+ diffusivity in pristine RP particles is in the order of $10^{-15} \text{ cm}^2 \text{ s}^{-1}$. Upon lithiation ($0 < x < 0.5$), a noticeable decrease of approximately an order of magnitude is observed. This could be attributed to the formation of Li-poor phases such as LiP_7 and Li_3P_7 as predicted by Mayo et al. [28]. Nevertheless, no experimental observation of such phases has yet to be reported and no evident plateaus are present in the galvanostatic profile in this region (figure 1b). Further lithiation ($0.5 < x < 2.5$) results in a constant increase in diffusivity, associated with an almost linear increase in volume. A characteristic plateau centered around 0.9 V vs Li^+/Li can be observed in the galvanostatic profile. In this range, Mayo et. al predict the formation of LiP and its conversion to Li_3P . The final drop in diffusivity can be related to the completion of the reaction and the formation of Li_3P .

The Na^+ diffusivity in a sodium-RP alloy displays a similar trend to that of Li^+ thus suggesting a similar reaction pathway. The more modest initial diffusivity decrease ($0 < x < 0.5$) could be attributed to the larger ionic radius of Na^+ leading to a lower initial diffusion. The average diffusivity, however, is higher than Li^+ , possibly because of the larger volume expansion upon sodiation. A similar plateau is observed in the galvanostatic profile, but at the lower voltage (0.3 V vs Na^+/Na) (figure 1c)

corresponding to the formation of Na_3P .

Potassium shows a contrasting trend, suggesting a different alloying mechanism. When K alloys with RP ($x < 0.3$) an initial drop in diffusivity of more than an order of magnitude can be observed (from 10^{-15} to $10^{-17} \text{ cm}^2 \text{ s}^{-1}$). As the concentration increases ($0.3 < x < 0.6$) the diffusivity suddenly increases to $10^{-15} \text{ cm}^2 \text{ s}^{-1}$ followed by a final drop for $x > 0.6$. The galvanostatic profile in (figure 1d) shows three different plateaus similar to predictions by Yang et al. suggesting they correspond to the formation of intermediate phases before forming the final KP phase.[29] This electrochemical behaviour is well reported in literature for both black phosphorus and RP. [4, 22] The potassium concentration in these phases ($x = 0.27, 0.66$ and 1) matches the changes in diffusivity we observed in our experiment, suggesting those changes could be indication of complete phase formation during the reaction. However, a more in-depth study is required to further confirm the formation of such phases.

Mechanical properties

Critical to understanding the role of deformation is to investigate the reversible change, characterized by elastic modulus (E) and Poisson's ratio (ν), and the irreversible change, characterized by fracture toughness (K_{IC}) and yield stress (σ_{yield}). Powder compression tests were conducted on commercially available RP powder to find the elastic and plastic response of the material. This approach was selected as no macroscopic fully dense sample of RP is available for mechanical testing, so a powder at range of densities was considered. Each unloading curve in figure 2a shows different volumes for a range of masses and therefore indicative of the powder as a material with different densities/porosities. This means the effect of volume fraction can be taken into account by solving equation (3) to find the fully dense bulk modulus, $B_0 = 1.9 \pm 0.1 \text{ GPa}$ [34]

$$B = B_0 e^{\left(-a \left(1 - \frac{\rho}{\rho_0}\right)\right)} \quad (3)$$

This value is slightly lower than those reported previously however it is the first measurement by a mechanical test rather than by digital imaging or x-ray diffraction. [25, 26]

The loading curves are characteristic of the powder being compressed under an increasing pressure P ; low pressures are related to the reorientation and

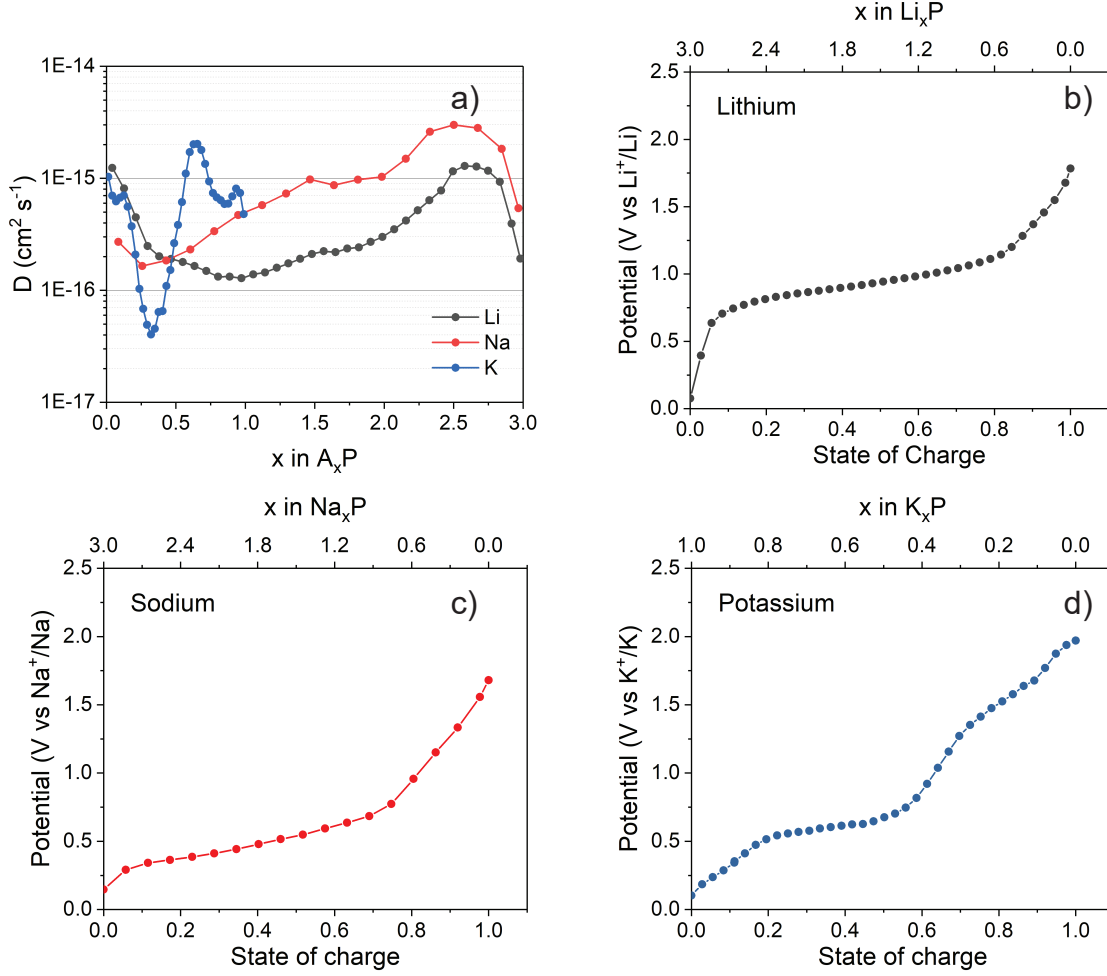


Figure 1: a) Diffusivity values for lithium, sodium and potassium in RP, calculated using the GITT profiles shown in the supporting information (figure S2 and Table S6) and equation (7). (b-d) charging profiles of (b) Li, (c) Na and (d) K made using steady state potentials taken from the GITT profiles in figure S2.

Elastic Property	B	Er	E	ν
Method	powder compression	ex-situ indent	calculated	calculated
RP	1.9 ± 0.1 GPa	2.5 ± 0.4 GPa	2.3 ± 0.4 GPa	0.296 ± 0.079
Amorphous Si	n.a.	n.a.	136 ± 9 GPa	0.27 ± 0.02
Plastic Property	σ_{yield}	H	$3H \approx \sigma_{\text{yield}}$	K_{1C}
Method	powder compression	ex-situ indent	calculated	in-situ
RP	500 ± 130 MPa	100 ± 50 MPa	290 ± 50 MPa	0.3 ± 0.1 MPa m ^{0.5}
Amorphous Si	9.2 ± 0.2 GPa	10.9 ± 0.9 GPa	33 ± 3 GPa	4.7 MPa m ^{0.5} $\pm 8\%$

Table 1: Elastic and Plastic properties of RP as measured and calculated by this work and values for amorphous silicon from references for comparison [30–33]

compaction of particles. High pressures give a linear response which can be fitted and related to particles yielding locally. Using multiple compression tests

(figure 2b), an average yield stress of the material can be calculated using the following equation [35]:

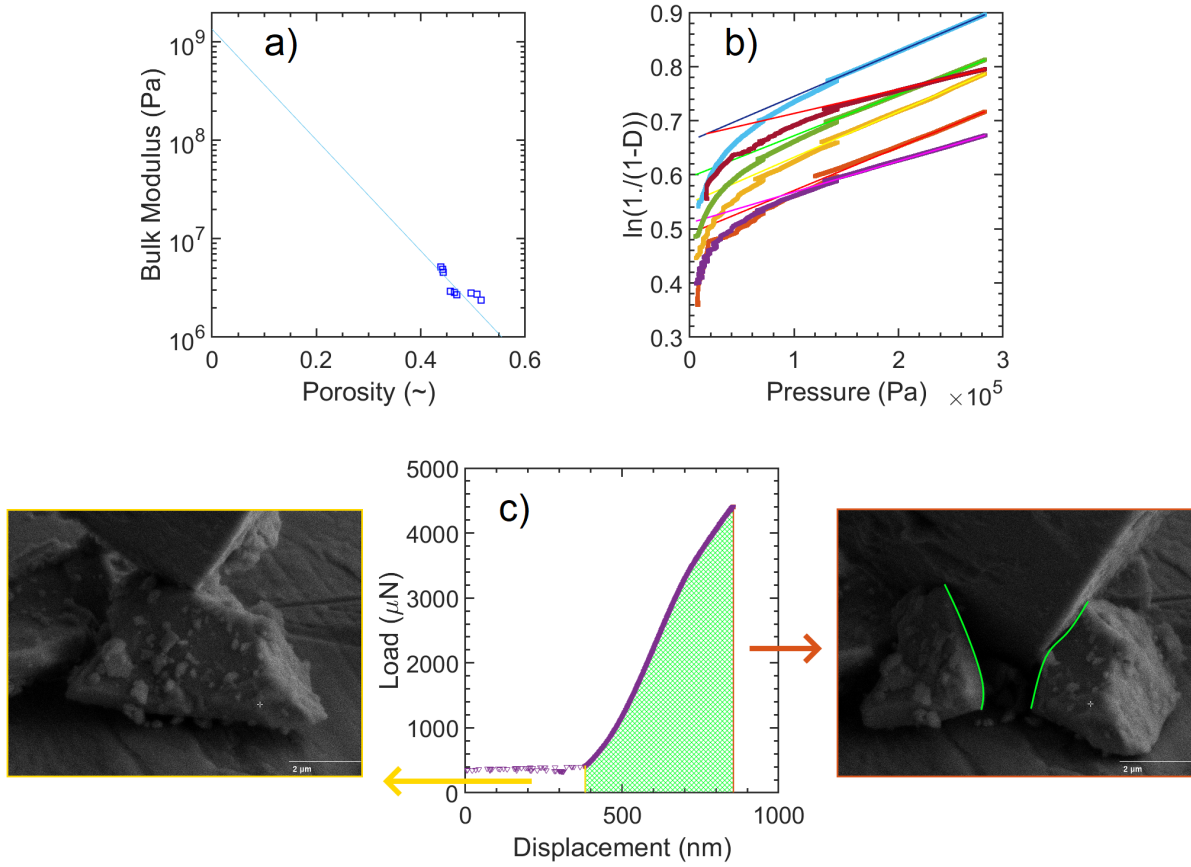


Figure 2: a) Bulk modulus measured from unloading of compacted powder at different porosities ($1 - \frac{\rho}{\rho_0}$) fitted to equation (3) where fully dense bulk modulus is the y-intercept, b) Heckle plot from compression of different amounts of RP powder fitted to find yield stress for each test equation (4), c) start-to-fracture energy and SEM images from in-situ test showing the surface before the fracture (left) and after the fracture (right), taken from Video_SI01.

$$\ln\left(\frac{1}{1-\rho}\right) = \frac{P}{3\sigma_{\text{yield}}} \quad (4)$$

The average measured value of σ_{yield} is found to be 500 ± 130 MPa, which is significantly lower than the yield strength of amorphous silicon ($\approx 1/20$ th). When considering failure of a particle, yield (plastic deformation) is an irreversible change in shape which, for continuity of electrical contact and coulombic efficiency, is preferable to fracture.

Ex-situ nanoindentation utilising constant stiffness measurements were performed to find the elastic modulus and the Poisson's ratio of RP. Nanoindentation experiments provide hardness H

(related to yield) and reduced elastic modulus, E_r , of the material, which is a combination of the mechanical properties of the sample and the indenter (the relevant equations can be found in the Supporting Information). Using the known instrument properties of the nanoindenter (elastic modulus, E_i , and Poisson's ratio, ν_i) and the reduced elastic properties of the material (E_r and B), we can calculate the previously unreported values necessary for the model i.e. E and ν (relevant equations in the Supporting Information).

In-situ secondary electron microscopy (SEM) nanoindentation of individual particles allowed for direct observation of cracking and therefore

the calculation of the fracture toughness (K_{IC}) via fracture surface area analysis, S measured directly from images, and the energy to fracture (F) corresponding to the area under the force-displacement curve in figure 2c [36].

$$K_{IC} = \sqrt{E \frac{dF}{dS}} \quad (5)$$

The values found experimentally by powder compression and nanoindentation are listed in table 1 and typical values of amorphous silicon are added for context. The plastic properties (yield vs fracture) show that RP can be categorised, like silicon, as a ceramic (chart 7 in [37]). The difference comes when considering both elastic moduli and plastic properties. Compared to Si, P can withstand higher strains (percentage volume change) without failure due to the significantly smaller elastic moduli ($\approx 1/60$ th). These values also allow for calculation of a critical flaw size which would lead to particle fracture rather than yield. For RP it is $160 \pm_{28}^{332}$ nm and for amorphous Si it is 6 ± 1 nm. These can be related to the possible size of particle that will fracture using the model in the following section.

Electrochemo-mechanical model

With the measured experimental parameters, we are now able to simulate the evolution of stresses in the RP during the alloying reaction. The model is built based on the assumptions that all parameters including diffusion coefficient, elastic moduli and partial molar volume are concentration independent, and that ions flow into the particle homogeneously from the surface of a spherical particle. In this way, we can obtain analytical solutions as shown in supporting information (Section 1). Notice should be taken that it may underestimate stress level for potassium, which shows distinct variations in the diffusion coefficient (as shown in figure 1). This may indicate a phase separation and thus high stress concentration at phase interfaces. For the calculation we take a spherical RP particle with radius of 100 nm and Young's modulus of 2.3 GPa.

The current density applied on the particle surface is the pore-wall current density (i_n) [38], which is approximated from

$$i_n = \frac{iR_0}{3\epsilon\delta_{\text{electrode}}} \quad (6)$$

for an electrode consisting of identical spherical active particles with radius R_0 . In equation (6), ϵ denotes

the volume fraction of RP in the electrode and $\delta_{\text{electrode}}$ is the electrode thickness. In an electrode with a thickness of 15 μm and a volume fraction of RP of 0.4, a current density of 10 mA cm^{-2} corresponds to a pore-wall current density of $i_n = 0.05 \text{ mA cm}^{-2}$, which is used for the calculation of figure 3a-c.

Figure 3a shows that radial stresses at the centre increases as ions insert into the particle and reaches a steady state. Potassium induces the highest stresses and lithium the lowest. At steady state, $Dt/R_0^2 > 0.25$, the radial and tangential stress distributions are shown in figure 3b, which shows that stress distribution is most homogeneous during lithiation and least homogeneous in the case of potassiation.

The radial stresses are always in tension and zero at the particle surface. The transverse (hoop) stresses change from a large tensile stress at the centre of the particle to a large compressive stress at the surface. This compressive stress will only lead to plastic failure (above σ_{yield}) and the tensile stresses will cause cracking or plastic failure depending on which failure stress is lower (σ_{1c} vs σ_{yield}). For clarity we have ignored any effect of phase formation throughout the model so a constant diffusivity value for each ion is used. As shown in figure 1, while Li and Na show a similar trend in change of diffusivity, K shows a more variable diffusivity ranging from 10^{-17} to $10^{-15} \text{ cm}^2 \text{ s}^{-1}$ (when $0.25 < x < 0.6$ in K_xP). We do expect then that the concentration gradient that would develop in regions with such concentrations will give rise to further stresses that are not taken into account in our model.

Figure 3c and d show how the size of the particles and the current density affect the maximal radial stresses. As outlined by the equation (1) this is a positive linear relationship in both cases but the gradient of increase is dictated by the ion used. This indicates that, although RP is capable of cycling with three alkali metals, the stresses in the particles caused by K would be the same as the ones experienced with Li alloying at a current density ≈ 3 times higher. The result is that RP can withstand the alloying with Li better than Na or K without experiencing a failure, i.e. $\sigma > \sigma_{\text{yield}}$. Figure 3e) shows the relationship between particle radius and pore-wall current which gives rise to the critical stress. Illustrating to increase one the other needs to be reduced and the limit line for failure above which the particle will yield/fracture. Additionally the lower stress on the particle during the alloying with Li shows that the critical failure stress is formed for a bigger critical

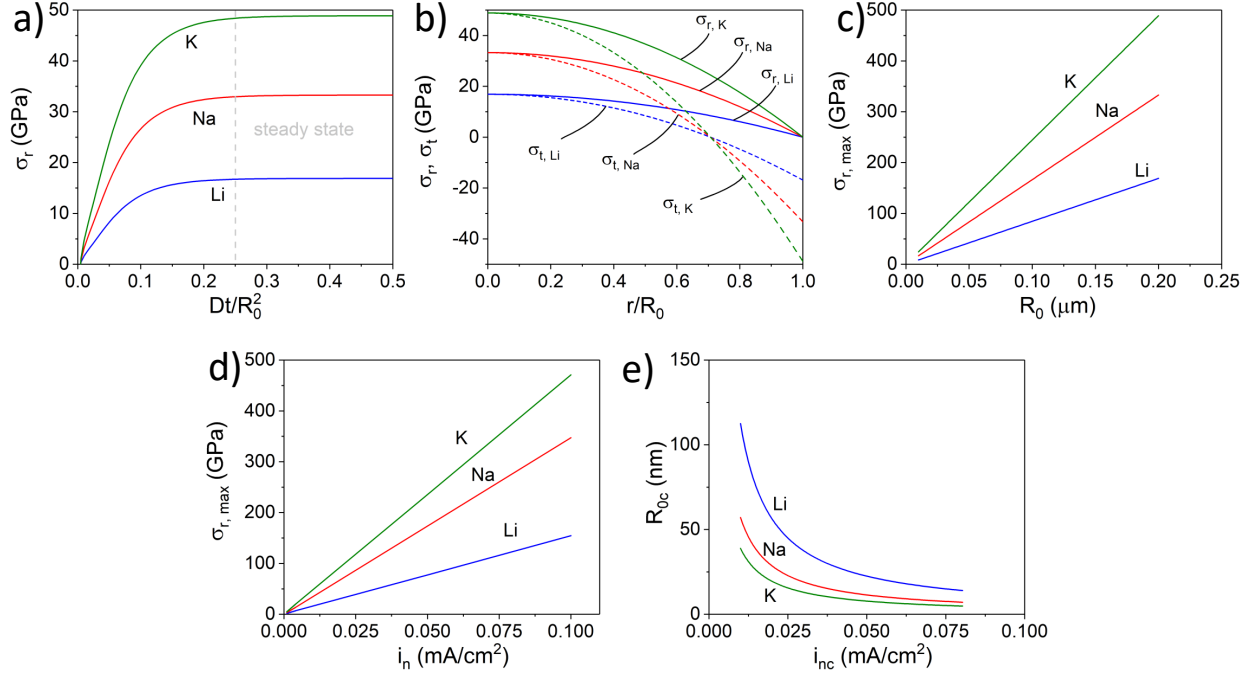


Figure 3: a) Evolution of radial stress with time normalised by diffusion rate (D) and particle size (R_0). b) Distribution of radial (solid line) and tangential (dashed line) stress within a sphere at steady state. c) and d) show the maximal radial stress with changing particle size and pore-wall current density respectively. e) Critical particle radius of RP when alloying with Li, Na and K when different pore-wall currents are applied.

particle size, R_{0c} , compared to the alloying with the other two alkali metals at the same critical pore-wall current, i_{nc} (figure 3e). Although the use of high currents is expected to decrease the critical particle size, the trend remains unchanged. These plots and the measured failure properties tell us that fracture can only start internally which is why fracture leads to catastrophic particle failure.

To consider the validity of this we performed an in-situ TEM study to charge particles at extreme current densities in the section below.

In-situ TEM: spherical RP particles

In order to validate the prediction of the model, we used an open cell setup to experimentally observe the volume expansion of chemically synthesized spherical RP particles (see Methods section) alloying under extreme charging conditions (figure 4).[39] Based on the density of RP and its alloys (Li_3P , Na_3P and KP), theoretical volume expansions of 168%, 331% and 162% are expected for the alloying reaction with Li, Na and K respectively (see Supporting Information).

Figure 4a,d,g show the expansion experienced by

spherical RP particles when they alloy with lithium (Video_SI02), sodium (Video_SI03) and potassium (Video_SI04). In all spherical particles, we observed a similar lengthening of both axes during alloying, confirming that the expansion was isotropic and observed no clear cracking. This suggests that spherical geometry and a small starting particle size suppresses crack formation despite high charging rate and highly directional flux of ions. Measuring particle size before and after lithiation (Figure 4c) showed an increase by a factor of 1.27 ± 0.04 , resulting in an average relative volume expansion of $105 \pm 20\%$. This value is lower than expected (168%), suggesting incomplete lithiation or the presence of a thin (< 15 nm) oxide layer not clearly visible in this experimental configuration. During sodiation, the diameter of the particles increased on average of 1.47 ± 0.09 times (figure 4f thus resulting in a volume expansion of $217 \pm 60\%$. This value is again lower than expected (331%), possibly for similar reasons to lithiation. For potassiation, the poorer image contrast made the particle size analysis more challenging. The diameter of the particles increased

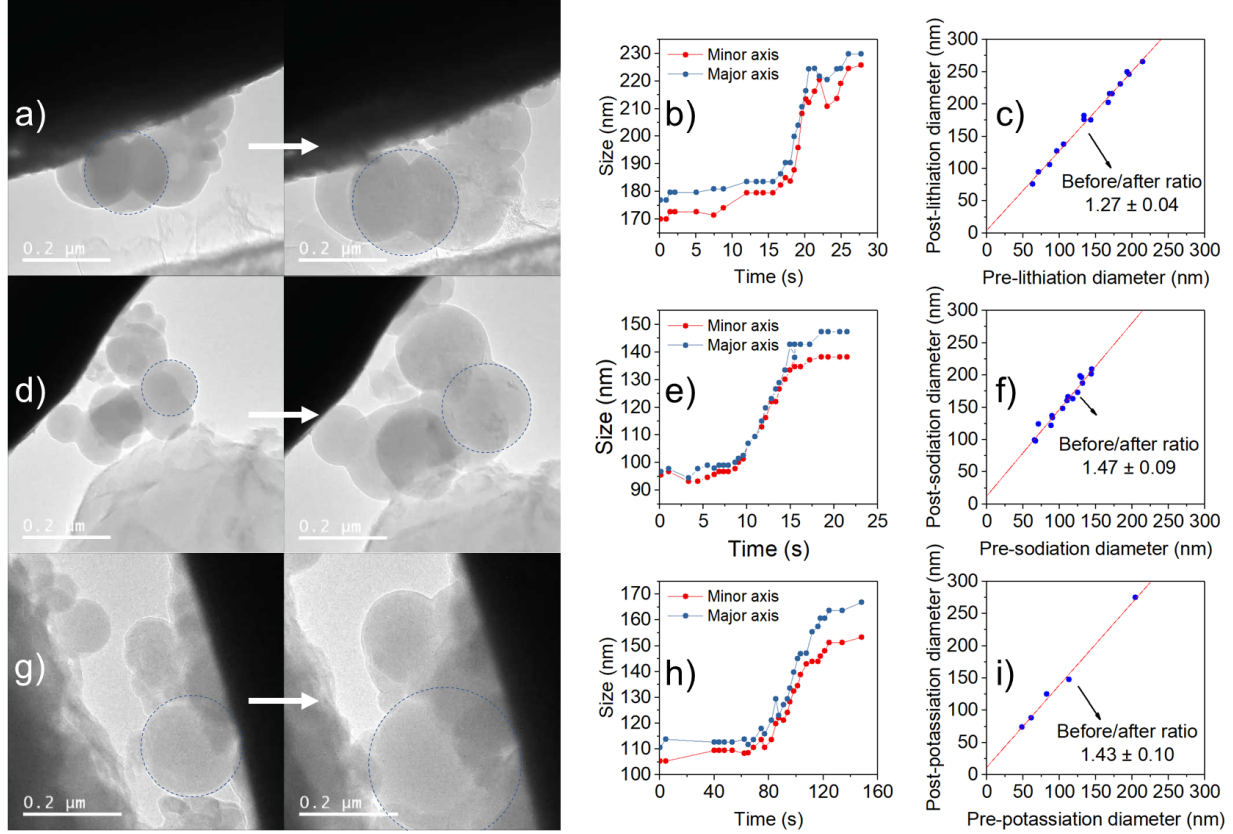


Figure 4: In-situ TEM experiments performed on spherical RP particles. a) before (left) and after (right) lithiation reaction. b) size change of the particle with time. c) average size change of the diameter of the particles after the alloying reaction. (d-f) and (g-i) show the data collected from the same experiment using sodium and potassium, respectively.

by 1.43 ± 0.10 times, resulting in a volume expansion of $192 \pm 60\%$. In this case, the expected value (162%) lies in the range observed.

In-situ TEM: ball milled RP particles

Ball milled commercial RP particles were also tested in-situ. TEM imaging (Figure 5) shows these particles are oblate, larger and have a rougher surface. The calculated volume expansion of these particles were different to the spherical case with volume changes of 72%, 179% and 217% for Li, Na and K respectively, but this difference is attributable to error in the assumed particle dimension perpendicular to the imaging plane (depth = width assumed), and the possible presence of an oxide layer (Video_SI05). A layer is visible around the particles with a sharp change in contrast from a brighter coating to a

darker particle core. The brighter surface layer is caused by less electron scattering; indicating a different composition. This layer's thickness remains unchanged after the completion of the alloying reaction, which supports the conclusion of it being a secondary inactive material layer, such as an oxide.

The main difference to the spherical case is the apparent crack at the surface of the particle formed during both lithiation and potassiation, highlighted in the central frame of figure 5a), positioned, relative to the point of contact for ion flux, near the 2 or 10 o'clock position. These cracks grow instantaneously to a length of ≈ 50 nm before crack growth is arrested.

As shown in figure 3 the stresses due to sodiation within a spherical particle should be greater than the lithiation case so we suggest that the lack of cracking in this example is an effect of the geometry and loading direction, with the sodium particle charged from point contact on its long side, instead of on its

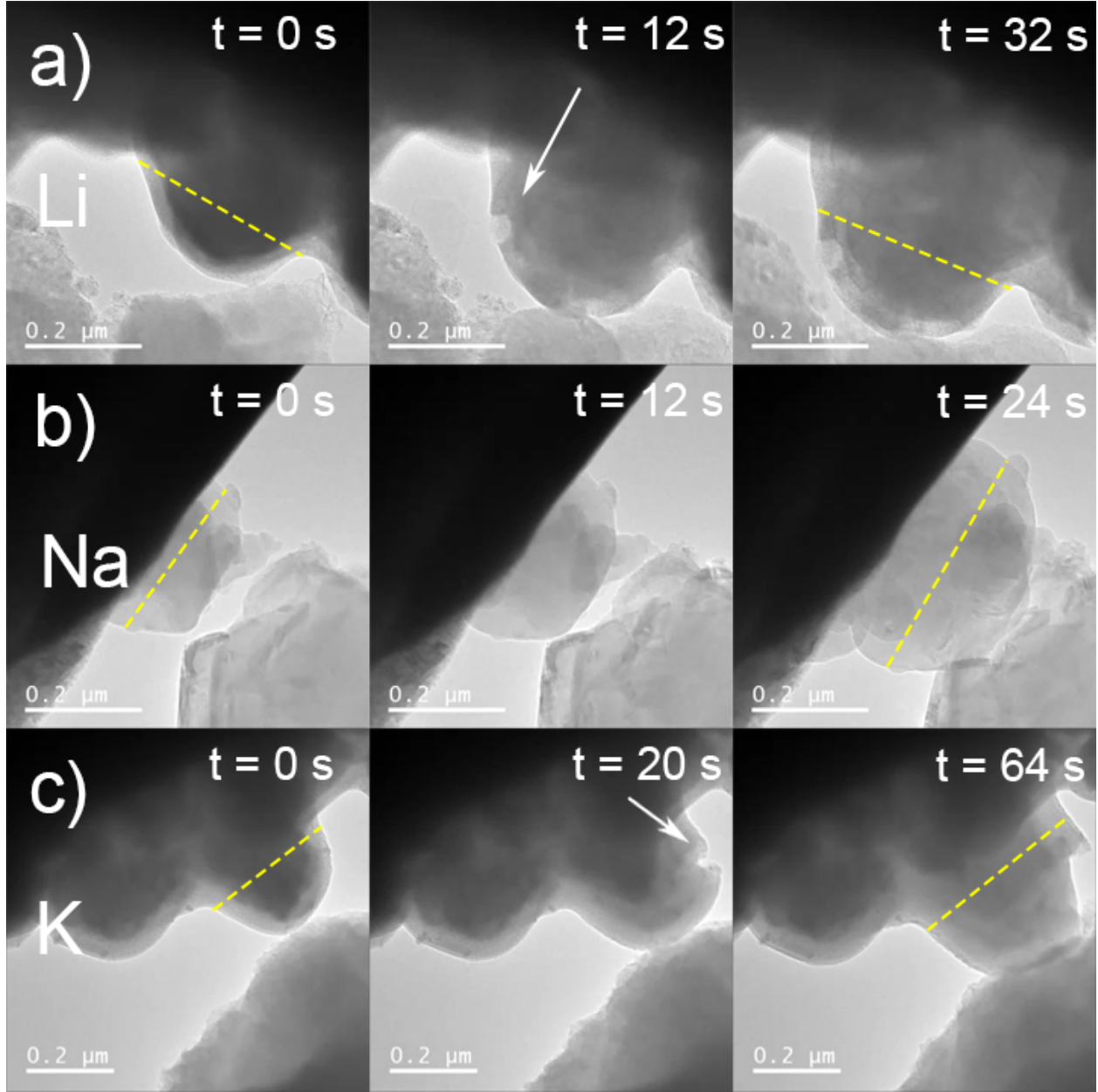


Figure 5: In-situ TEM experiments performed on ball milled commercial RP. Frames taken from Video_SI05, Video_SI06 and Video_SI07, showing lithiation, sodiation and potassiation of the particles, respectively. The sequence from left to right shows the beginning of the experiment and the end of the reaction, respectively. The alkali metals that are used are lithium (a), sodium (b) and potassium (c). The white arrows point to the newly formed surface cracks on the particles. The yellow dashed lines show the axis that were measured to calculate the volume expansion.

short side, leading to a lower stress concentration.

Crucially of both cracking cases, neither is catastrophic. This could be due to three reasons. First, the stress concentration at the tip leads to

plastic yielding and blunting of the crack tip. Second, the stresses that expansion generates at the surface of a particle, which our modelling shows are compressive in the tangential direction, will perturb mode I

cracking, figure 3. Third, the scale of the cracks and halo of different TEM contrast reveals at a secondary possible reason for cracking. These cracks could be the cracking of native oxide layer on the particle and not the RP. The oxide on commercial RP has been shown to be of the $\approx 15\text{-}50\text{ nm}$ scale [21, 40]. This may be present because these particles were produced from commercial RP and, although the preparation of the sample was made in inert atmosphere, a noticeable oxide can still be present. An oxide layer of this magnitude is not present on the spherical particles because they are chemically synthesized and proper care was taken to avoid exposure to air. Regardless, even in this extreme charging, ball milled case, catastrophic failure of red phosphorus is avoided, as predicted by its mechanical properties.

In-situ TEM experiment modelling

Finally we consider the effect of geometry and ion flux positioning with our model for the two cases observed with oblate spheroids, figure 6. This case considers ions entering a particle from one point and so there is an effect of diffusion that leads to a positional gradient of expansion (i.e. the point the ions enter will expand before the rest of the particle) and this leads to a tensile stress illustrated in the figure by colour. This shows that the stress at the surface at the 2-10 o'clock position on the oblate loaded from the narrow end can be double that when entering from the long edge. This would contribute to the normal expansion stresses and could lead to fracture. However, it is important to note that this is both an extreme case (directional loading) and a time dependent effect which will reduce quickly as the expansion continues throughout the particle. This mirrors the finding that the cracks observed do not propagate as their driving force has been removed.

Conclusions

In summary, we show the development of a model that calculates the stresses experienced by an alloying particle illustrated with the example of RP with Li, Na and K. The development of this model required the study of the mechanical and electrochemical properties of RP, which were measured for the first time in this work. Our model highlights that increasing the charging current or particle size will increase the stresses associated with the volumetric

change as expected. However, the novelty lies in understanding where those stresses are at their maximum and the role of plasticity vs fracture. In the idealised case of a perfectly spherical particle with a uniform ion flux from the exterior the maximal stresses are internal. This means a RP particle would need a flaw of $\sim 160\text{ nm}$ or bigger within a particle with size and current defined by the line in figure 3e to fail by fracture. This means if we assume particles of commercially available RP with a $10\text{ }\mu\text{m}$ diameter, figure S3b (value taken from the mode of the particle-size distribution of commercial RP), alloyed with a Lithium pore-wall ion current density of $\sim 1.5\text{ }\mu\text{A cm}^{-2}$ (macro current density $15\text{ }\mu\text{A cm}^{-2}$ equation (6)) it will fail plastically, keeping electrical and ionic connection throughout, unless there is a $\geq 1.6\%$ flaw/pre-crack in the centre ($\geq 160\text{ nm}$). With modern particle production routes a flaw larger than 1% is unlikely so suggesting most working particles will not fracture during cycling. Considering it from a macro current density approach a 10 mA cm^{-2} would equate to an ideal pore-wall current density of $\sim 25\text{ }\mu\text{A cm}^{-2}$ with a critical radius of $\sim 40\text{ nm}$ (larger yields plastically) meaning an internal flaw/pre-crack which is bigger than the diameter would be needed for fracture. This further reinforces the idea that at moderate-to-high current with sensible particle sizes RP fails plastically during cycling. Therefore particle size and cycling rate are not limited by RP's fracture and focus can move to other variables for optimisation of cycling an anode: eg. surface area-to-volume ratios, electronic conductivity, composite ratios, electrode microstructure. We also validated our model by testing both spherical and ball-milled RP particle via in-situ TEM experiments under extreme conditions such as high C-rate and heterogeneous flow of ions. Our findings show that the spherical starting particles suppress crack formation, with cracks observed only on ball-milled particles. The non-spherical case illustrates that particle geometry can effect the stresses evolved during cycling, with the most extreme when linked with uni-directional ion flux. This case as observed and modeled leads to a high but transient stress which can initiate a crack but not propagate it. This is particularly evident for RP as it favours plastic failure which blunts crack tips, stopping the particle being split in two where a material with less plasticity would fail completely. The mechanical and electrochemical properties of RP shown in this paper and the model developed

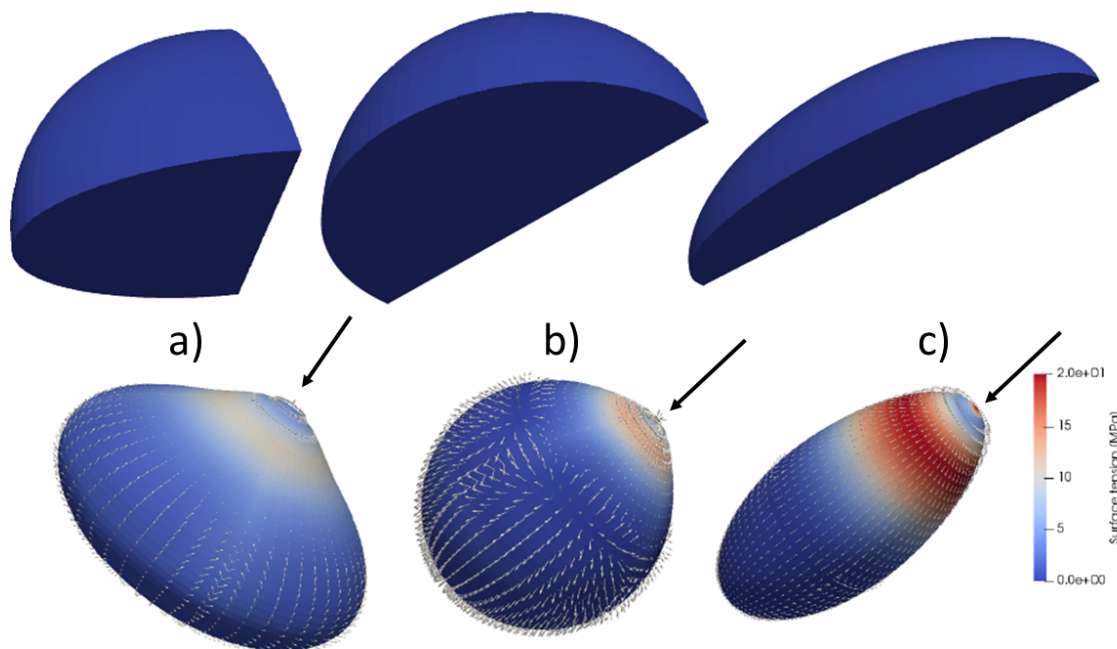


Figure 6: Modelling of RP alloying in in-situ TEM conditions (anisotropic flow of ions) and different particle geometry. (a) shows loading on a long edge of an oblate shaped particle, (b) on a sphere and (c) on a narrow edge of a prolate shaped particle. On the top row, a quadrant of the particle model is shown. on the bottom, the surface stresses of the corresponding cases are shown. The black arrows show the direction of the flow of the ions in the particle. The grey arrows on the surface of the particles show the directions of surface stresses, and the colored contour shows magnitudes of tensile stress along longitude direction.

have the potential to motivate future research into a material that not only has the ability to alloy with all the main alkali ions but also demonstrated a good resistance to catastrophic failure. Considering what has been learnt here we can speculate that if; capable of manufacturing near spherical particles with no internal flaws, then there is no size limit to which they can be charged using extremely high C-rates, with no fear of loss of electrical contact giving excellent cycling stability. This work highlights RP as a battery material and a method of investigation to give a new direction of the battery community. The authors hope others utilise this model and mode of holistic working to study future electrode materials recognising the role of mechanical properties in the cycle life of the material.

Methods

Synthesis of spherical RP particles

Spherical RP particles were synthesized following a procedure developed by Chang et al [41] The sample preparation of was done in a glovebox (MBraun) to prevent any exposure to air that would provoke the formation of a phosphorus oxide layer on the synthesized particles. A solution of PI_3 (99%, Sigma Aldrich) 1.5 M dissolved in iodobenzene (98%, Sigma Aldrich) was used as a phosphorus source. This solution was then added to a 0.016 M solution of cetyltrimethylammonium bromide (CTAB) (98%, Sigma Aldrich) in ethylene glycol (99.8%, Sigma Aldrich) under vigorous stirring. The solution was stirred for 30 minutes and then the powder was collected and washed three times with ethanol using a centrifuge. The sample was then kept under vacuum at 60 °C overnight to allow it to dry completely. This method allows the production of spherical RP

particles with a average size of 130 nm (figure S3b,e).

Synthesis ball milled RP particles

3.4 g of RP (powder, 98.9%, Alfa Aesar) were ball milled in a FRITSCH Pulverisette 7 using 180 zirconia balls (\varnothing 5 mm) in a 45 ml zirconia jar with the addition of 10 ml of ethylene glycol. The milling was operated for 60 h at 500 rpm. Compared to commercial RP, this method produces a sample with a particle size distribution greatly reduced, ranging from 100 nm up to 1 micron (figure S3b,c,d) while avoiding the conversion of RP to black phosphorus (confirmed by the absence of diffraction peaks in fig S3a), that can occur in such conditions [20]. This method is also described as the step 1 in a previously published paper [21] The surface area of the ball milled RP particles was measured through a BET analysis using a Micrometrics Tristar II 3020. The particle size distribution was measured using a Malvern Mastersizer 2000 DLS analyzer with two lasers (633 nm and 466 nm).

In-situ transmission electron microscopy of alloying

To fully comprehend the role of particle size and geometry, in-situ TEM tests were run with spherical RP particles produced by a synthetic procedure published by Chang et al and on commercial RP particles without the addition of any conductive agent or binder. [41] The in-situ electrochemical test was employed by using an FEI Tecnai G2 F20 X-Twin TEM at the acceleration voltage of 200 kV. Nanofactory Instruments Dual-Probe STM-TEM holder was used to apply bias between RP and Li, Na or K metal electrodes. Cu and W wires were used for RP and Li, Na or K metal parts as the working and counter electrodes, respectively. A relative bias of -1.5 V was induced between the two electrodes, which caused alkali ions to be transferred to the RP electrode through the natural oxide layer on the metal tip acting as a solid electrolyte. A schematic of the experiment is shown in figure S7. In-situ TEM video frames were analysed using the ellipse tool in ImageJ to manually measure particle dimensions at each frame.

Electrochemical test

To measure the diffusivity of RP, we manufactured RP-graphite electrodes following a previously

published procedure [21] 0.7 g of ball milled RP were mixed with 0.3 g of graphite (SFG6, TIMCAL) in a stainless steel jar for 48 h with 5 stainless steel balls (\varnothing 1 cm) at 500 rpm under argon gas to obtain a composite with 7/3 phosphorus to carbon ratio. To prepare the electrode, the composite, Super P conductive carbon (TIMCAL) and Polyacrylic acid binder (450kDa, Sigma Aldrich) were mixed in a ratio 8:1:1 in a glovebox using NMP as the solvent to obtain a slurry. The slurry was cast on copper foil and let dry overnight to allow the evaporation of the solvent. Later, the casting was dried at 100 under vacuum overnight to completely remove any trace of solvent. 10 mm \varnothing electrodes were cut from the casting and used for the electrochemical tests. The P mass loading was about 1-1.2 mg cm⁻². The electrodes were tested in triplicate in coin cells where lithium, sodium and potassium metal disks were used as counter and reference electrodes.

The electrolytes used in the experiments are listed in table 2:

Alkali ion	Li	Na	K
Electrolyte	LiPF ₆ 1M in EC:DEC	NaPF ₆ 1M in EC:DEC + FEC 10%	KFSI 1M in EC:DEC

Table 2: Electrolytes used for the electrochemical tests.

Hexafluorophosphates (PF₆⁻) of Li and Na salts were selected as widely used in LIBs and NIBs applications. Due to the low solubility of KPF₆ (0.8M), KFSI was used instead. The addition of FEC 10% in the Na electrolyte was necessary to form a stable SEI and achieve reliable cycling and GITT electrochemical tests.[42]

The electrochemical performance of this material with Li, Na and K are shown in figure S8. The C-rates in each experiment were calculated based on the theoretical capacity of RP with each alkali metal (2596 mAh g⁻¹ for Li and Na and 865 mAh g⁻¹ for K. Currents applied range from C/20 to 1C.

To calculate the diffusivity of the alkali ions in RP, the following equation was used:

$$D = \frac{4}{\pi} \left(\frac{i\Omega_M}{Z_{AFS}} \right)^2 \left[\frac{(dV_{ss}/d\delta)}{(dV_{ca}/d\sqrt{t})} \right]^2 \left(\tau \ll \frac{L^2}{D} \right) \quad (7)$$

where i is the current applied, Ω_M is the molar volume of the electrode material calculated at each step ($\text{cm}^3 \text{ mol}^{-1}$), Z_A is the charge number, F is the Faraday constant (96485 C mol^{-1}), S is the electrode/electrolyte contact area (cm^2), $dV_{ss}/d\delta$ is the difference of potential after subsequent steady state steps (V_{ss}), $dV_{ca}/d\sqrt{t}$ is the slope of the linearized plot of the potential while the current is applied (V_{ca}) versus \sqrt{t} . τ is the time duration of the current pulse and L is the characteristic length of the electrode. However, RP suffers from a very low electronic conductivity ($10^{-14} \text{ S cm}^{-1}$) which hinders the use of GITT that requires the electron transfer to be fast enough compared with alkali-ion transport so that electrons can always equilibrate at any time instant [43]. The use of a RP-graphite composite on one hand is necessary to make sure that this condition is satisfied. This composite was prepared with a 7/3 phosphorus-to-carbon mass ratio following a procedure stated in the Methods based on the following assumptions [21]. First, we assume that the RP particles are the only active material in the electrode and that the particles are separated. With this assumption, we state that the current is only interacting with RP and that the electrode/electrolyte contact area is mainly related to the surface area of RP. In this way, the electrolyte/electrode contact area can be calculated from the surface area of the ball milled RP, measured with BET ($22.9 \text{ m}^2 \text{ g}^{-1}$, see Methods), multiplied by the mass of RP present on the electrode tested during the experiment. Second, we assume that the diffusivity of lithium and potassium in graphite is orders of magnitude faster than in RP ($\approx 10^{-9} \text{ cm}^2 \text{ s}^{-1}$ for lithium and $\approx 10^{-8} \text{ cm}^2 \text{ s}^{-1}$ for potassium in graphite) [44, 45]. This is particularly true in the sodium case where the alkali ion does not intercalate at all in graphite. [46] For this reason we assume that the diffusivity values we obtain from the experiment are mainly related to the diffusivity of the ions in RP. GITT experiments were performed applying a current to the active material for 30 minutes, followed by a resting period of two hours (figure S2). The electrodes were all discharged to 0.01 V vs Li, Na and K to allow the formation of the SEI and then charged to 2.5 V vs Li, Na and K at C/20. When dealloying, a current of C/20 was applied for 30 minutes and the system was allowed to reach a steady state potential for 2 hours before the new pulse.

Mechanical properties characterisation

Nanoindentation

The fundamental question of how the RP particles break/fail comes down to how the material responds to stress. The two main failure modes of any material is via fracture (brittle) or yield (plasticity). To measure these failure modes on a particle scale both in-situ and ex-situ nanoindentation were conducted on commercially available RP powder. In-situ tests within a Mira 3 Tescan with a PI 88 Hysitron picoindenter allowed for observation of particle cracking and calculation of a fracture toughness, K_{IC} , via fracture area analysis and energy to fracture, a and b in figure 2. Ex-situ tests using a G200 Agilent (KLM) utilising constant stiffness measurements to find an elastic modulus, E , and hardness H (related to yield), the equations behind which can be found in the supplementary information.

Powder compression tests

To verify the results found on a single particle scale powder compression tests were conducted on commercially available RP powder to find the elastic and plastic response of the material. Using an Instron test rig and a simple die and punch, powders of known weights were compressed under displacement control. Each sample was loaded to 50 N, 100 N and 200 N with unloading to $< 5 \text{ N}$ between each step to generate a set of three loading and three unloading curves per powder. The loading curves are indicative of the powder being compressed and particles yielding locally so can be analysed with a Heckle plot to find the yield strength of the material figure 2c. ([35]). Each unloading curve is indicative of the powder as a material with different densities so the effect of volume fraction must be taken into account to produce the bulk modulus, B figure 2d. [34] To be able to make these analyses the density of the powder tested must be known to a high tolerance. Therefore, the density of RP was measured using a OHAUS Pioneer Density Kit. Ethanol was used as a solvent and, in order to measure the density of the RP powder, the density of empty vials was measured prior to the addition of the sample, full details on the density calculation can be found in the supplementary information.

Data Availability

The authors declare that all data supporting the findings of this study are included within the paper and its Supplementary Information files. Source data are available from the corresponding author upon reasonable request.

Acknowledgements

The authors would like to acknowledge the financial support of the ISCF Faraday Challenge project SOLBAT [grant number FIRG007] and the Henry Royce Institute (through UK Engineering and Physical Science Research Council grant EP/R010145/1) for capital equipment. I.C. acknowledges support from a Modentech studentship. H.-W.L. acknowledge the 2019 Research Fund (1.190031.01) of Ulsan National Institute of Science and Technology and Individual Basic Science Engineering Research Program (NRF-2019R1C1C1009324) through the National Research Foundation of Korea funded by the Ministry of Science and ICT. We are grateful to the David Cockayne Center for Electron Microscopy for the use of their electron microscopes.

Author Contributions

I.C., E.D. and M.P. conceived and designed the experiments. I.C. prepared the samples and measured the electrochemical properties. E.D. and J.A. measured the mechanical properties of RP. Y.Z. developed the electrochemo-mechanical model and performed the calculations. T.-U.W. and H.-W.L. performed the in-situ TEM lithiation experiments and provided guidance on the interpretation in-situ data. I.C., J.A., E.D. and M.P. wrote the manuscript with input from all authors. The project was supervised by M.P.

References

1. Goodenough, J. B. & Kim, Y. Challenges for Rechargeable Li Batteries†. English. *Chem. Mater.* **22**, 587–603 (2009).
2. Janek, J. & Zeier, W. G. A solid future for battery development. *Nature Energy* **1**, 16141 (2016).
3. Tarascon, J. M. & Armand, M. Issues and challenges facing rechargeable lithium batteries. *Nature* **414**, 359–367 (2001).
4. Chang, W. C., Wu, J. H., Chen, K. T. & Tuan, H. Y. Red Phosphorus Potassium-Ion Battery Anodes. *Advanced Science* **6** (2019).
5. Kim, Y. *et al.* An amorphous red phosphorus/carbon composite as a promising anode material for sodium ion batteries. *Advanced Materials* **25**, 3045–3049 (2013).
6. Sun, Y. *et al.* Design of Red Phosphorus Nanostructured Electrode for Fast-Charging Lithium-Ion Batteries with High Energy Density. *Joule* **3**, 1080–1093 (2019).
7. Wiberg, E., A.F., H. & Wiberg, N. *Inorganic Chemistry* 1884 (Academic Press, 2001).
8. Dey, A. N. Electrochemical Alloying of Lithium in Organic Electrolytes. *Journal of The Electrochemical Society* **118**, 1547 (1971).
9. Rahman, M. A., Song, G., Bhatt, A. I., Wong, Y. C. & Wen, C. Nanostructured silicon anodes for high-performance lithium-ion batteries. *Advanced Functional Materials* **26**, 647–678 (2016).
10. Teki, R. *et al.* Nanostructured silicon anodes for lithium Ion rechargeable batteries. *Small* **5**, 2236–2242 (2009).
11. Wu, H. & Cui, Y. Designing nanostructured Si anodes for high energy. *Nano Today* **7**, 414–429 (2012).
12. Yoshio, M. *et al.* Carbon-Coated Si as a Lithium-Ion Battery Anode Material. *Journal of The Electrochemical Society* **149**, A1598 (2002).
13. Liu, X. H. *et al.* Size-dependent fracture of silicon nanoparticles during lithiation. *ACS Nano* **6**, 1522–1531 (2012).
14. Li, Y. *et al.* Growth of conformal graphene cages on micrometre-sized silicon particles as stable battery anodes. *Nature Energy* **1** (2016).
15. Zhao, Y. *et al.* A review on modeling of electro-chemo-mechanics in lithium-ion batteries. *Journal of Power Sources* **413**, 259–283 (2019).
16. Zhang, S., Zhao, K., Zhu, T. & Li, J. Electrochemomechanical degradation of high-capacity battery electrode materials. *Progress in Materials Science* **89**, 479–521 (2017).

17. Itou, Y. & Ukyo, Y. Performance of LiNiCoO₂ materials for advanced lithium-ion batteries. *Journal of Power Sources* **146**, 39–44 (2005).
18. Bucci, G., Swamy, T., Chiang, Y.-M. & Carter, W. C. Random Walk Analysis of the Effect of Mechanical Degradation on All-Solid-State Battery Power. *Journal of The Electrochemical Society* **164**, A2660–A2664 (2017).
19. Koerver, R. *et al.* Capacity Fade in Solid-State Batteries: Interphase Formation and Chemomechanical Processes in Nickel-Rich Layered Oxide Cathodes and Lithium Thiophosphate Solid Electrolytes. *Chemistry of Materials* **29**, 5574–5582 (2017).
20. Ramireddy, T. *et al.* Phosphorus-carbon nanocomposite anodes for lithium-ion and sodium-ion batteries. *Journal of Materials Chemistry A* **3**, 5572–5584 (2015).
21. Capone, I., Hurlbutt, K., Naylor, A., Xiao, A. & Pasta, M. Effect of the Particle-Size Distribution on the Electrochemical Performance of a Red Phosphorus-Carbon Composite Anode for Sodium-Ion Batteries. *Energy and Fuels* **33** (2019).
22. Sultana, I., Rahman, M. M., Ramireddy, T., Chen, Y. & Glushenkov, A. M. High capacity potassium-ion battery anodes based on black phosphorus. *Journal of Materials Chemistry A* **5**, 23506–23512 (2017).
23. Xiong, P. *et al.* Red Phosphorus Nanoparticle@3D Interconnected Carbon Nanosheet Framework Composite for Potassium-Ion Battery Anodes. *Small* (2018).
24. Huang, X. *et al.* Phosphorus/Carbon Composite Anode for Potassium-Ion Batteries: Insights into High Initial Coulombic Efficiency and Superior Cyclic Performance. *ACS Sustainable Chem. Eng* **6**, 16308–16314 (2018).
25. Rissi, E. N., Soignard, E., McKiernan, K. A., Benmore, C. J. & Yarger, J. L. Pressure-induced crystallization of amorphous red phosphorus. *Solid State Communications* **152**, 390–394 (2012).
26. Zaug, J. M., Soper, A. K. & Clark, S. M. Pressure-dependent structures of amorphous red phosphorus and the origin of the first sharp diffraction peaks. *Nature Materials* **7**, 890–899 (2008).
27. Zhu, Y. & Wang, C. Galvanostatic intermittent titration technique for phase-transformation electrodes. *Journal of Physical Chemistry C* **114**, 2830–2841 (2010).
28. Mayo, M., Griffith, K. J., Pickard, C. J. & Morris, A. J. Ab Initio Study of Phosphorus Anodes for Lithium- and Sodium-Ion Batteries. *Chemistry of Materials* **28**, 2011–2021 (2016).
29. Yang, W., Lu, Y., Zhao, C. & Liu, H. First-Principles Study of Black Phosphorus as Anode Material for Rechargeable Potassium-Ion Batteries. *Electronic Materials Letters* **16**, 89–98 (2020).
30. Hopcroft, M. A., Nix, W. D. & Kenny, T. W. What is the Young’s modulus of silicon? *Journal of Microelectromechanical Systems* **19**, 229–238 (2010).
31. Domnich, V., Aratyn, Y., Kriven, W. M. & Gogotsi, Y. Temperature dependence of silicon hardness: Experimental evidence of phase transformations. *Reviews on Advanced Materials Science* **17**, 33–41 (2008).
32. Petersen, K. Silicon as a mechanical material. *Proceedings of the IEEE* **70**, 420–457 (1982).
33. Chen C. P. Leipold, M. H. Fracture toughness of silicon. *American Ceramic Society Bulletin* **59**, 469–472 (1980).
34. Rice, R. W. *Porosity of Ceramics* (CRC Press, 2017).
35. Heckel, R. W. Density-Pressure Relationships in Powder Compaction (1961).
36. Zehnder, A. T. in, 185–219 (2012).
37. Weaver, P. M. *Materials Selection in Mechanical Design*. by Michael F Ashby United Kingdom, 1999.
38. Doyle, M., Fuller, T. F. & Newman, J. Modeling of Galvanostatic Charge and Discharge of the Lithium/Polymer/Insertion Cell. en. *Journal of The Electrochemical Society* **140**, 1526–1533 (1993).
39. Zhang, X., Lee, S. W., Lee, H.-W., Cui, Y. & Linder, C. A reaction-controlled diffusion model for the lithiation of silicon in lithium-ion batteries. *Extreme Mechanics Letters* **4**, 61–75 (2015).

40. Marino, C., El Kazzi, M., Berg, E. J., He, M. & Villevieille, C. Interface and Safety Properties of Phosphorus-Based Negative Electrodes in Li-Ion Batteries. *Chemistry of Materials* **29**, 7151–7158 (2017).
41. Chang, W.-C., Tseng, K.-W. & Tuan, H.-Y. Solution Synthesis of Iodine-Doped Red Phosphorus Nanoparticles for Lithium-Ion Battery Anodes. *Nano Letters* **17**, 1240–1247 (2017).
42. Dahbi, M. *et al.* Black Phosphorus as a High-Capacity, High-Capability Negative Electrode for Sodium-Ion Batteries: Investigation of the Electrode/Electrolyte Interface. *Chemistry of Materials* **28**, 1625–1635 (2016).
43. Wang, R. *et al.* Influence of Conductive additives on the stability of red phosphorus-carbon anodes for sodium-ion batteries. *Scientific Reports* **9**, 1–6 (2019).
44. Wang, S., Xu, H., Li, W., Dolocan, A. & Manthiram, A. Interfacial Chemistry in Solid-State Batteries: Formation of Interphase and Its Consequences. *Journal of the American Chemical Society* **140**, 250–257 (2018).
45. Levi, M. D. & Aurbach, D. Diffusion coefficients of lithium ions during intercalation into graphite derived from the simultaneous measurements and modeling of electrochemical impedance and potentiostatic intermittent titration characteristics of thin graphite electrodes. *Journal of Physical Chemistry B* **101**, 4641–4647 (1997).
46. Moriwake, H., Kuwabara, A., Fisher, C. A. & Ikuhara, Y. Why is sodium-intercalated graphite unstable? *RSC Advances* **7**, 36550–36554 (2017).